Contents lists available at ScienceDirect

# Food Chemistry: X

# Integration of covalent organic frameworks and molecularly imprinted polymers for selective extraction of flavonoid naringenin from grapefruit (*Citrus × paradisi* Macf.) peels

Xiumei Chen, Yingying Sheng, Jinxin Che [*], Okwong Oketch Reymick, Nengguo Tao [*]

*School of Chemical Engineering, Xiangtan University, Xiangtan 411105, PR China*

ABSTRACT

Grapefruit (*Citrus × paradisi* Macf.) peel, a by-product of the citrus-processing industry, possesses an important economic value due to the richness of bioactive compounds. In this study, boron-linked covalent organic frameworks integrated with molecularly imprinted polymers (CMIPs) were developed via a facile one-pot bulk polymerization approach for the selective extraction of naringenin from grapefruit peel extract. The obtained CMIPs possessed a three-dimensional network structure with uniform pore size distribution, large surface areas ($476 \ m^2/g$), and high crystallinity. Benefiting from the hybrid functional monomer APTES-MAA, the acylamino group can coordinate with the boronate ligands of the boroxine-based framework to form B-N bands, facilitating the integration of imprinted cavities with the aromatic skeleton. The composite materials exhibited a high adsorption capacity of 153.65 mg/g, and a short adsorption equilibrium time of 30 min for naringenin, together with favorable selectivity towards other flavonoid analogues. Additionally, the CMIPs captured the template molecules through $\pi$–$\pi^*$ interaction and hydrogen bonding, as verified by FT-IR and XPS. Furthermore, they had good performance when employed to enrich naringenin in grapefruit peels extract compared with the common adsorbent materials including AB-8, D101, cationic exchange resin, and active carbon. This research highlights the potential of CMIPs composite materials as a promising alternative adsorbent for naringenin extraction from grapefruit peel.

## 1. Introduction

Grapefruit (*Citrus × paradisi* Macf.) is a crucial member of the Citrus genus within the Rutaceae family and has extensive applications in the juice and food industry. However, industrial processing of citrus fruit results in significant waste, with approximately 50 % of its wet mass being comprised of discarded citrus peel (Stabrauskiene et al., 2022). Grapefruit peels are rich sources of valuable compounds, including various flavonoids, vitamin C, fiber, pectin, essential oils, polyphenols, and important levels of some trace elements (Mahmoud et al., 2019). Naringenin (5,7-dihydroxy-2-(4-hydroxyphenyl) chroman-4-one) belongs to the flavonoid class and is well known for its beneficial health properties such as antioxidants, antimicrobial, antimutagenic and anti-cancer (Gercek et al., 2021). A number of extraction methods such as liquid–liquid extraction (Barbosa et al., 2021), a fungal NRPS-PKS enzyme that catalyzes the synthesis of flavonoid naringenin (Zhang et al., 2022), and macroporous resin adsorption methods (Nasir et al.,

2019) had been reported. They usually involve the use of large quantities of hazardous solvents, time-consuming or nonselective. To address this issue, molecularly imprinted polymers (MIPs) might be a good choice.

MIPs are synthesized through the radical co-polymerization of template molecules that are covalently or non-covalently conjugated with functional monomers, cross-linking agents, and comonomers, which can form the imprinted cavities with shape locations, sizes, and functional groups that are chemically and physically complementary to template molecules, thereby enabling the re-identification of target molecules. Owing to their high affinity and specificity, MIPs have received much attention in recent years and have been widely used in aspects of separations, analysis of synthetic food dyes (Hatamluyi et al., 2021) and pesticide residues (Zhang et al., 2021), and flavonoids enrichment (e.g. caffeic acid and cyanidin-3-O-glucoside) in complex foodstuff matrices (Nasir et al., 2019; Zhao et al., 2020). Their efficiency highly depended on the number of recognition sites and surface area in them, which

limited their uses to a large extent. Covalent organic frameworks (COFs) integrated with the MIPs may be a solution. COFs are a versatile class of crystalline porous polymers that allow the atomically precise integration of organic units to form predesigned skeletons, tuneable pore structures, and high surface areas (Grunenberg et al., 2021). They offer great opportunities as a new platform for designing promising organic materials for catalysis, gas storage, adsorption (Hao et al., 2021), drug delivery (Gan et al., 2019), active substances extraction and enrichment (Zhao et al., 2020). Recently, the unique combination of COFs with multifunctional monomers (**Liu et al., 2018), carbon quantum dots nanoparticles (Qi et al., 2021), MoS$_2$ nanosheets (Sun et al., 2019), and metal–organic frameworks integrate the advantage of both materials (Zhang et al., 2021). In terms of single MIPs, the flexible skeletons (C—C bonds) tend to distort and aggregate into dense structures leading to a decreased binding affinity and specificity for target molecules (Wang et al., 2022). Based on the inherent aromatic rigid skeleton of COFs, the incorporation of MIPs into COFs could effectively prevent the deformation or collapse of the imprinted cavities and ensure the accuracy of the recognition sites (Zhao et al., 2020). Additionally, COFs typically contain an sp$^2$-hybridized orbit structure and considerable delocalized π bond at a large scale that promotes the hydrophobicity and π–π* interactions between COFs and target compounds containing phenyl groups, thereby preventing hydration and improving the stability of target compounds during separation (Liu et al., 2021). The functional monomer is also one of the key factors to achieve high-performance materials. Compared to the conventional monomer, the organic–inorganic hybrid monomer as a new functional monomer combines the advantages of organic and inorganic monomers, which can offer high mechanical stability.

For the reason given above, a strategy of fusion covalent organic frameworks and molecularly imprinted polymers was developed for preparing CMIPs, with hybrid functional monomer (APTES-MAA), by a facile one-step polymerization process. The CMIPs were synthesized using naringenin as the template, 3-aminopropyltriethoxysilane-methacrylic acid (APTES-MAA) as a hybrid functional monomer, benzene-1,4-diboronic acid (DBA) as precursor molecules of COFs, and ethylene glycol dimethacrylate (EGDMA) as the crosslinker and azobis (isobutyronitrile) (AIBN) as an initiator. The CMIPs polymers were characterized using SEM, FT-IR, XRD, BET, TGA, and XPS. A series of batch adsorption experiments were carried out to investigate their adsorption behaviors and selectivity of CMIPs/CNIPs for naringenin. Finally, taking advantage of their remarkable adsorption capacity and excellent adsorption selectivity, CMIPs were further evaluated for their high-efficiency enrichment of naringenin from real grapefruit (*Citrus × paradisi* Macf.) peels.

## 2. Experimental sections

### 2.1. Chemicals and materials

Naringenin standards (≥98 %) were purchased from Sigma-Aldrich (Shanghai, China). N, *N*-dimethylformamide (DMF), acetic acid, HPLC-grade methanol, and acetonitrile were obtained from Kemiou Chemical Reagent Co., Ltd. (Tianjin, China). benzene-1,4-diboronic acid (DBA), 1,4-dioxane, mesitylene, methacrylic acid (MAA), ethylene glycol dimethacrylate (EGDMA), 3-aminopropyltriethoxysilane (APTES), azobis (isobutyronitrile) (AIBN), anthocyanin, rutin, hesperidin, and baicalin were purchased from Aladdin Reagent Co., Ltd. (Shanghai, China). Acetone, anhydrous ethanol, and anhydrous methanol were supplied by Beijing Chemical Reagent Company (Beijing, China). AB-8, D101, and cationic exchange resin were obtained by Donghong Chemical Co., Ltd. (Shandong, China). Active carbon was made in the laboratory. Ultra-pure water was obtained using a Milli-Q water purification system (Millipore, Bedford, MA, American). Unless otherwise stated, all the other chemicals were of analytical reagent grade and were used without further purification.

Grapefruits (*Citrus × paradisi* Macf.) were purchased from a local market in Xiangtan City, Hunan province on May 7$^{th}$, 2021.

### 2.2. Preparation of CMIPs

The template molecules naringenin (32.67 mg) and MAA (41.32 mg) were added into acetonitrile (10 mL) and stirred magnetically at 45 °C for 4 h to obtain a homogeneous solution. Subsequently, APTES (75.27 mg), DBA (250 mg), and a 10 mL mesitylene/dioxane solution (1:1, v/v) were added to the above solution and sonicated for 60 min to form a prepolymer. The cross-linker EGDMA (1982.2 mg) and the initiator AIBN (44.34 mg) were then added into the mixture dropwise. After being deoxygenated with N$_2$ for 10 min, the mixed solution was transferred to a stainless-steel autoclave and heated to 70 °C for 24 h. The resulting precipitate was then filtered and washed with acetone, anhydrous methanol, and DMF, respectively, to remove the unreacted residuals. The naringenin was removed by Soxhlet extraction with a solution of methanol-acetic acid (v/v, 9:1) several times until there was no template detected by HPLC. The CNIPs were prepared in the same way in the absence of naringenin.

### 2.3. Characterization

Field emission scanning electron microscope (SEM) images were taken using Sigma300 (Zeiss, Germany) and INSPECT F50 (FEI, American), Energy dispersive X-ray (EDX) analysis and elemental mapping were collected using an energy-dispersive X-ray spectroscope attached to OCTANE SUPER, the Brunauer Emmett Teller (BET) measured by Quantachrome NOVA Instruments (Quantachrome Instruments Corp., American), and Fourier transform infrared (FT-IR) spectra (4000–400 cm$^{-1}$) recorded on a NICOLET 380 (Thermo Nicolet Corp., American) at a scanning speed of 4 cm$^{-1}$. X-ray diffraction (XRD) pattern was obtained by Bruker D8 Advanced Diffractometer System, equipped with Cu Kα radiation (40 kV, 40 mA), and the thermo-gravimetric analysis (TGA) measurement was performed using a Netzsch STA 429 thermoanalyser operating at a heating rate of 10 °C/min in alumina crucibles from room temperature to 900 °C under an air atmosphere. Inductively coupled plasma mass spectrometry (ICP-MS) was recorded on a NexION 300X (PerkinElmer Corp., American).

### 2.4. HPLC analysis of naringenin

Naringenin and flavonoid analogues including rutin, hesperidin, anthocyanin, and baicalin were quantified by high-performance liquid chromatography (HPLC) using a Shimadzu LC-15C system liquid chromatograph (Santa Clara, CA, American), equipped with ZORBAX SB-C18 chromatographic column (4.6 × 250 mm, 5 μm; Agilent, American) and SPD-15C UV-detector (Shimadzu, Japan). For naringenin analysis, the mobile phase was methanol (A) and 0.2 % aqueous acetic acid (B). Gradient elution was applied as below 0–5 min, 30 % A; 5–10 min, 30–85 % A; 10–17 min, 85–100 % A; 17–27 min, 100–100 % A; 27–29 min, 100–30 % A; 29–35 min, 30 % A. The flow rate, injection amount, column temperature, and detection wavelength were 1.0 Ml/min, 20 μL, 40 °C, and 289 nm, respectively. All solutions used for HPLC were filtered through a 0.22 μm membrane filter.

### 2.5. Adsorption experiments

A stock solution of naringenin of 500 mg/L was prepared in a mixture of ethanol and deionized water. Appropriate dilutions (v:v) of the stock solution were made with deionized water to obtain working solutions. For the pH experiments, the initial pH of a 20 mg/L naringenin solution was adjusted to the range of 3.0–9.0 using 0.1 mol/L HCl and 0.1 mol/L NaOH. Adsorption kinetics experiments were carried out by introducing 10.0 mg of CMIPs or CNIPs adsorbents into a 50 mL solution containing 40 mg/L naringenin. At different time intervals, the

adsorbents were separated and subsequently, the supernatant was analyzed by HPLC to determine the concentration of naringenin. The adsorption capacity of naringenin was calculated according to Eq. (1):

$$q_t = \frac{(C_0 - C_t)}{m} V \tag{1}$$

where $q_t$ (mg/g) represents the equilibrium adsorption capacity of naringenin, $C_0$ (mg/L) and $C_t$ (mg/L) are concentrations of naringenin at initial and time $t$ (min); $V$ (L) and $m$ (g) are the volumes of solutions and the mass of adsorbents, respectively.

For the adsorption isotherm experiments, 10.0 mg of absorbents were added to each naringenin solution with concentrations ranging from 20 to 400 mg/L and subsequently transferred to dark places where they were shaken at different temperatures (288–308 K) for 4 h. The residual concentration of naringenin in the solutions was then determined after reaching equilibrium. The adsorption capacity and imprinting factor (*IF*) were calculated according to Eqs. (2) and (3), respectively.

$$q_e = \frac{(C_e - C_0)}{m} V \tag{2}$$

$$IF = \frac{q_{CMIPs}}{q_{CNIPs}} \tag{3}$$

where $q_e$ (mg/g) is the amount of naringenin adsorbed at equilibrium; $C_e$ (mg/L) and $C_0$ (mg/L) are the initial and final concentrations of naringenin; $V$ (L) and $m$ (g) are the volumes of solutions and the mass of adsorbents, individually; $q_{CMIPs}$ (mg/g) and $q_{CNIPs}$ (mg/g) are the adsorption capacities of CMIPs and CNIPs adsorbents.

### 2.6. Selectivity and regeneration experiments

The selectivity of CMIPs and CNIPs was compared using naringenin and its analogues, including hesperidin, anthocyanin, rutin, and baicalin. Specifically, 10.0 mg of CMIPs and CNIPs were incubated in 50 mL solutions containing 25 mg/L of naringenin or its analogues. The mixtures were shaken in a thermostatic oscillator at 25 °C for 2 h to make sure the binding equilibrium was reached. The concentrations of all test flavonoids in the supernatant were determined by HPLC. Further experimental details can be found in SI. The distribution ratio $K_d$ and selectivity coefficient $k^{sel}$ were calculated according to Eqs. (4) and (5), respectively.

$$K_d = \frac{Q_e}{C_e} \tag{4}$$

$$k^{sel} = \frac{K_{d,template molecule}}{K_{d,referent molecule}} \tag{5}$$

where $Q_e$ (mg/g) and $C_e$ (mg/L) represent the equilibrium adsorption capacity and concentration of corresponding flavonoids, respectively. Naringenin is selected as a template molecule while other flavonoids serve as reference molecules. $K_{d,template\ molecule}$ and $K_{d,referent\ molecule}$ are the distribution ratio of template molecule and referent molecules.

The reusability of CMIPs/CNIPs was investigated through six cycles of desorption-adsorption cycles using the same procedure as the static adsorption experiment. After reaching equilibrium, naringenin-loaded CMIPs/CNIPs were collected by centrifugation and eluted with a mixed solvent of methanol/acetic acid (9:1, v/v). The recovered adsorbent was then thoroughly washed with ethanol to remove any residual naringenin before being reused for subsequent adsorption experiments. All the experiments were performed in triplicates.

### 2.7. Application of the CMIPs to real samples

Grapefruit peel extract was used to verify the feasibility of CMIPs.

The fruits were washed, manually peeled, sliced into long strips, and dried at 50 °C in a conventional oven reaching a stable dry weight. A mixture of 2.5 g crushed grapefruit peel powder and 10 mL petroleum ether was thoroughly blended and left to stand in a brown jar for 8 h. The mixture was filtered through a qualitative filter paper, then mixed with ethanol in a round-bottom flask and refluxed at 85 °C for 2 h before being concentrated by rotary. The resulting extract was stored in a 4 °C refrigerator before analysis. To 10.0 mg of CMIPs in a 50 mL conical flask, 20 mL of naringenin extract (100 mg/mL) was added and left for 24 h, after which the CMIPs were eluted with 50 mL of 80 % ethyl alcohol for 2 h. The content of naringenin in grapefruit peel extraction was determined using the aforementioned HPLC method.

### 2.8. Statistical analysis

Each experiment was repeated three times, and the reported results were processed using the SPSS statistical software package (10.1, SPSS Inc., USA). Significant differences were calculated using analysis of variance (ANOVA) with 0.05 of significance level. Graphs were prepared using Origin 8.0 software.

## 3. Results and discussion

### 3.1. Preparation and characterization

A strategy of fusion covalent organic frameworks and molecularly imprinted polymers was developed for preparing CMIPs, with hybrid functional monomer (APTES-MAA), by a facile one-step polymerization process (Scheme 1). Among various COFs, COF-1, whose structure consists of benzene rings linked by $B_3O_3$ into hexagon-shaped 2D sheets, was selected. The CMIPs were synthesized using naringenin as the template, 3-aminopropyltriethoxysilane-methacrylic acid (APTES-MAA) as a hybrid functional monomer, benzene-1,4-diboronic acid (DBA) as precursor molecules of COFs, and ethylene glycol dimethacrylate (EGDMA) as the crosslinker and azobis (isobutyronitrile) (AIBN) as an initiator. Additionally, the APTES-MAA was obtained through a dehydration condensation, which is via catalyzing the formation of boroxine rings by forming a Lewis-type interaction with the electron-deficient boron, contributing acylamino group from APTES-MAA to form B-N coordination with boronate ligands (Shen et al., 2019), and endowed the CMIPs super high stability by forming a brønsted-type interaction with defect sites in COF-1 (Bao et al., 2021; Du et al., 2015).

Scanning electron microscopy (SEM) was used to investigate the morphology and hierarchical structure of CMIPs. As depicted in Fig. 1A and C, the porous structure of CMIPs exhibited higher dispersity and regularity compared to CNIPs, indicating that templates facilitated the arrangement of functional monomers (Zhao et al., 2020). The network structure of the encapsulated nanospheres was observed in both CMIPs and CNIPs (Fig. 1B and D). However, the pore structure of CMIPs exhibited a more uniform and regular pattern with an average diameter of approximately 2–4 nm, which could be attributed to the release of template cavities during extraction (Motia et al., 2021). The elements of B, C, N, O, and Si that made up CMIPs were observed through the energy-dispersive spectrometer analysis (Fig. S1) and the elemental mapping (Fig. 1a–e) verified the existence and homogeneously distribution of these elements. Furthermore, Si from APTES and B from COFs were successfully occupied with an atomic ratio of 11 % and 6 %, respectively. These results suggested a potential interaction between COFs and MIPs.

The $N_2$ adsorption–desorption isotherms of CMIPs and CNIPs were analyzed to determine their pore structure and surface areas. As shown in Fig. 2A, a typical type IV isotherm with a hysteresis loop behavior for CMIPs and CNIPs was observed. The specific surface area of CMIPs (476 $m^2$/g) was significantly higher than that of CNIPs (259 $m^2$/g), which can be attributed to the ordered arrangements of imprinted cavities during synthesis (Yang et al., 2017). The pore size distribution of CMIPs
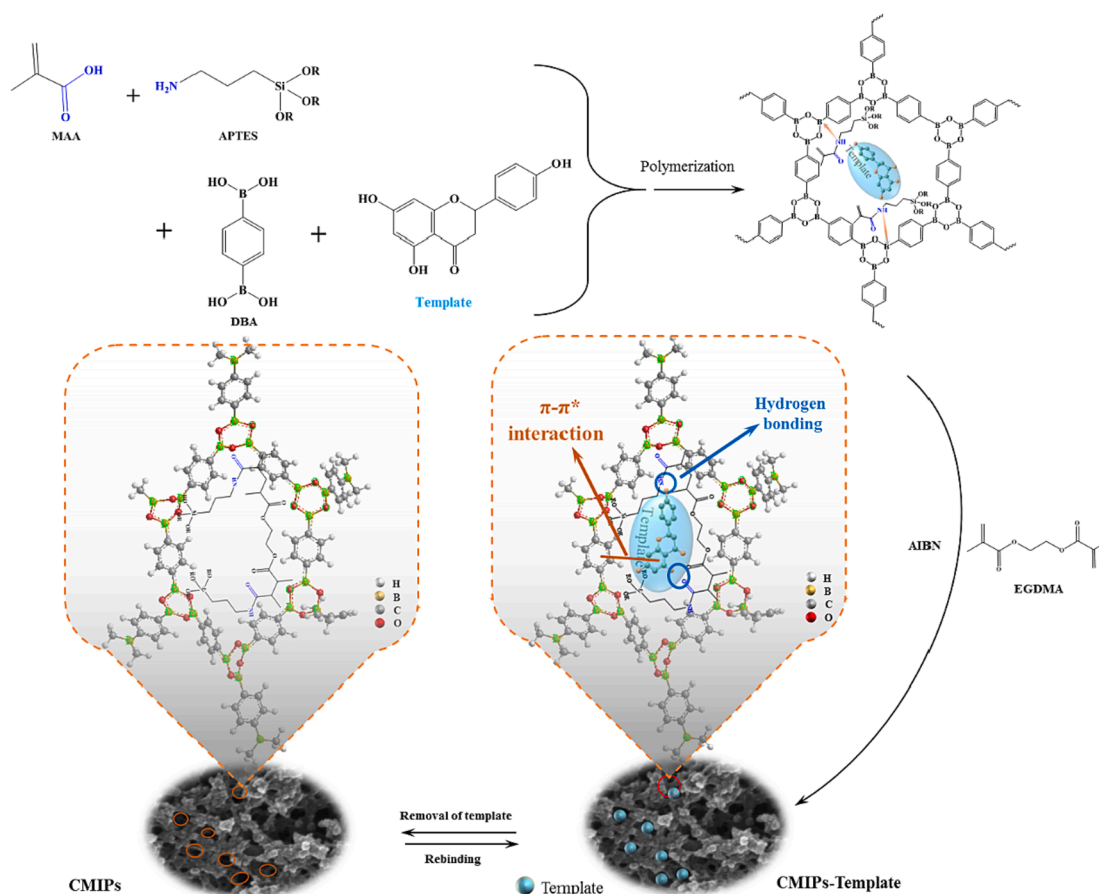
**Scheme 1.** The schematic diagram of the preparation of CMIPs.

(Fig. 2a) showed a concentrated peak at a pore diameter of 2.27 nm, indicating the existence of considerable mesoporous structure (Sun et al., 2021), which can provide excellent recognition sites for template molecules under free solvents and low pressures (Saad et al., 2021). Consequently, some imprinted cavities were found after the elution of the template molecules, which was consistent with the results of SEM images.

FT-IR analysis showed that the characteristic peak of CMIPs and CNIPs existed at 1631 cm$^{-1}$ (Fig. 2B), respectively, corresponding well to the typical C=O stretching vibration of amide groups. The amide groups (O=C-NH-) stemmed from the hybrid functional monomer APTES-MAA and the reaction equation for APTES-MAA was shown in Scheme S1. The absorption peaks at 1386 and 1039 cm$^{-1}$ represented the stretching vibration of the B-O and B-C bond (Gan et al., 2019), whereas those at 3440 and 2983 cm$^{-1}$ were the stretching vibration of the N—H in APTES-MAA and –CH$_3$ in EGDMA (Pan et al., 2020; Zhang et al., 2019b). These results confirmed the presence of the functional monomer and the cross-linker in the CMIPs.

To verify the crystallinity and structural integrity of CMIPs and CNIPs, the XRD analyses were performed. As shown in Fig. 2C, CMIPs and CNIPs have the same diffraction peaks at 28.3°, 32.8°, 47.2°, and 56.0°, indicating that the crystalline framework of CMIPs remained stable during the preparation of CMIPs (Lu et al., 2021; Sun et al., 2018). Interestingly, an amorphous diffraction pattern at 28° was observed in both CMIPs and CNIPs, which underlined that the amorphous silica was involved in the formation of the frameworks.

The thermal stabilities of CMIPs and CNIPs were compared by the thermogravimetric curves at 30–900 °C in an N$_2$ atmosphere (Fig. 2D). Results showed that the whole decomposition process for both CMIPs and CNIPs was divided into three main stages. Firstly, 5.01 % weight loss

occurred at 100 °C due to the removal of the residual solvent. Then, a rapid weight loss at 200–380 °C was observed, which was normally caused by the disintegration of the oxygen-containing functional groups (Wang et al., 2021). At last, when the temperature was above 380 °C, the thermal weight loss became moderate owing to the carbon dioxide release induced by the burning of carbon atoms in the framework (Zhang et al., 2019a). However, the DTG values of CNIPs were significantly lower than those of CMIPs, indicating that the thermal stability of CMIPs was higher than that of CNIPs.

### 3.2. Bach adsorption

#### 3.2.1. Effect of pH on the adsorption capacity of CMIPs

Given that both the surface binding sites of CMIPs and the chemical properties of naringenin were influenced by the pH of the sample solution, the effect of pH on the adsorption capacity of CMIPs was investigated. As shown in Fig. 3A, the adsorption capacity of CMIPs for naringenin gradually decreased from pH 3.0 to 6.0, and then remained nearly stable at pH 7.0. This phenomenon can be attributed to the fact that the carboxyl and hydroxyl groups would be deprotonated to form –COO$^-$ and -O$^-$ groups and thereby subduing non-covalent interactions between the functional group in the cavity and the naringenin molecules (Fazary et al., 2016). The sharp decline between pH 6.0–7.0 could also be caused by the weakened π–π* interaction between naringenin and CMIPs (Tang et al., 2020). In contrast, there was no difference in the adsorption capacity of CNIPs for naringenin under acidic and neutral conditions. The results showed that it could be used to recover naringenin from acidic media.
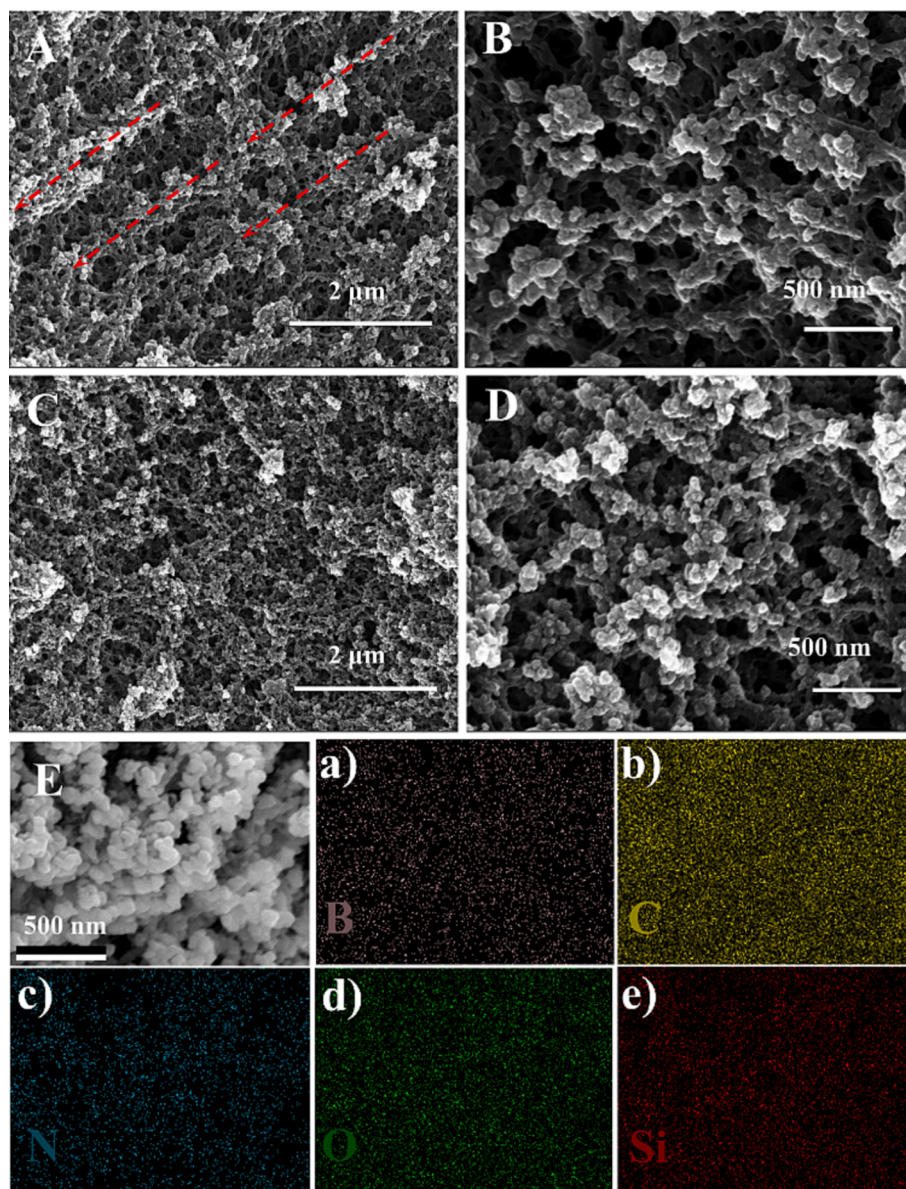
**Fig. 1.** SEM images of CMIPs (A, B) and CNIPs (C, D); SEM-EDX elemental mapping images of B (a), C (b), N (c), O (d) and Si (e) for CMIPs.

### 3.2.2. Effect of naringenin concentrations on the adsorption capacity of CMIPs

The uptake of naringenin by CMIPs was drastically influenced by the naringenin concentrations. As shown in Fig. 3B, concentrations of naringenin lower than 40 mg/L at 25 °C led to a rapid increase in the adsorption capacity of CMIPs. Similar results were also observed in CNIPs, but its peak value (113.60 mg/g) was significantly lower than that of CMIPs (198.26 mg/g). This result was consistent with those by SEM and BET analysis, which confirmed a previous report describing that the addition of template molecules could lead to the direct rearrangement of the functional monomers. It was the rearrangement that enabled imprinted cavities on the surface to specifically recognize and match the naringenin molecule in chemical structure and spatial arrangement (Zhao et al., 2020). Therefore, 40 mg/L was chosen as the optimum concentration for subsequent adsorption experiments.

### 3.2.3. Adsorption kinetics

The kinetics curves of CMIPs and CNIPs were shown in Fig. 3C. During the initial 30 min, the adsorption capacity increased rapidly. Then it increased gradually and reached its adsorption saturation (183.72 mg/g) at 90 min. This phenomenon can be caused by the considerable unoccupied cavities in CMIPs at initial adsorption whereas their number became poor with time prolonging and thus prevent the arrival of naringenin (Cui et al., 2020). To further investigate the potential mechanism the pseudo-first-order model (Eq. (6)), pseudo-second-order model (Eq. (7)), and intra-particle diffusion model (Eq. (8)) were applied to fit and analyze the experimental data.

$$ln(q_e - q_t) = lnq_e - k_1 t \tag{6}$$

$$\frac{t}{q_t} = \frac{1}{k_2 q_e^2} + \frac{t}{q_e} \tag{7}$$

$$q_t = k_3 t^{\frac{1}{2}} + c \tag{8}$$

where $t$ was the adsorption time (min); $q_e$ and $q_t$ were the theoretical adsorption capacities (mg/g) at equilibrium and the adsorption capacities (mg/g) at the time of $t$; $c$ was the intercept reflecting the effect of the boundary layer; $k_1$ (1/min), $k_2$ (g/mg/min) and $k_3$ (g/mg/min) represented the first-order rate constant, second-order rate constant and intra-particle diffusion rate constant, respectively.
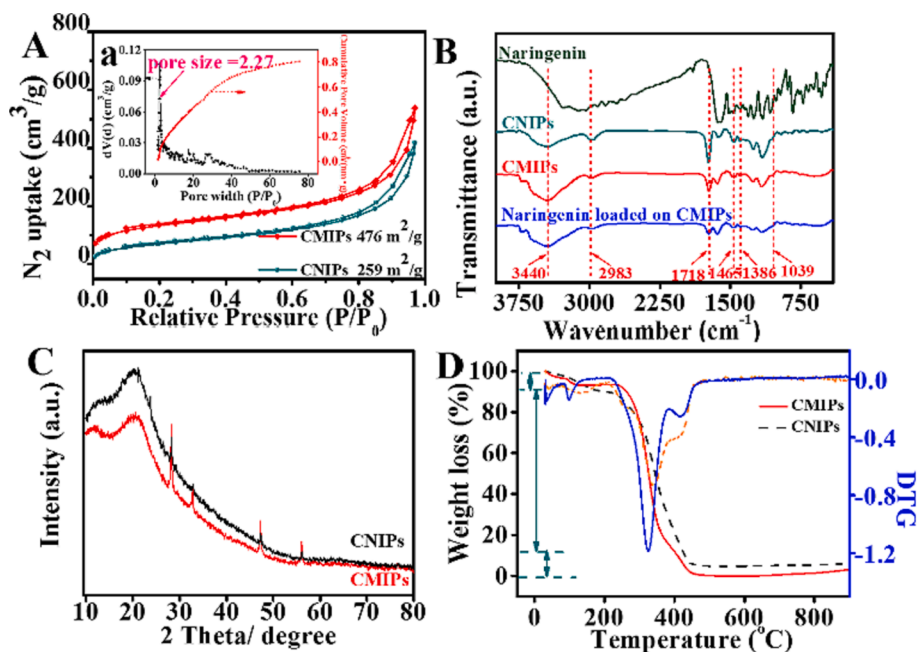
**Fig. 2.** (A) $N_2$ adsorption isotherms of CMIPs and CNIPs at 77 K, with the inset (a) showing the pore size and volume distribution of CMIPs; (B) FT-IR spectra of naringenin, CNIPs, CMIPs, and naringenin loaded on CMIPs, (C) the XRD patterns of CMIPs and CNIPs, and (D) the TGA and DGA curves of CMIPs and CNIPs.
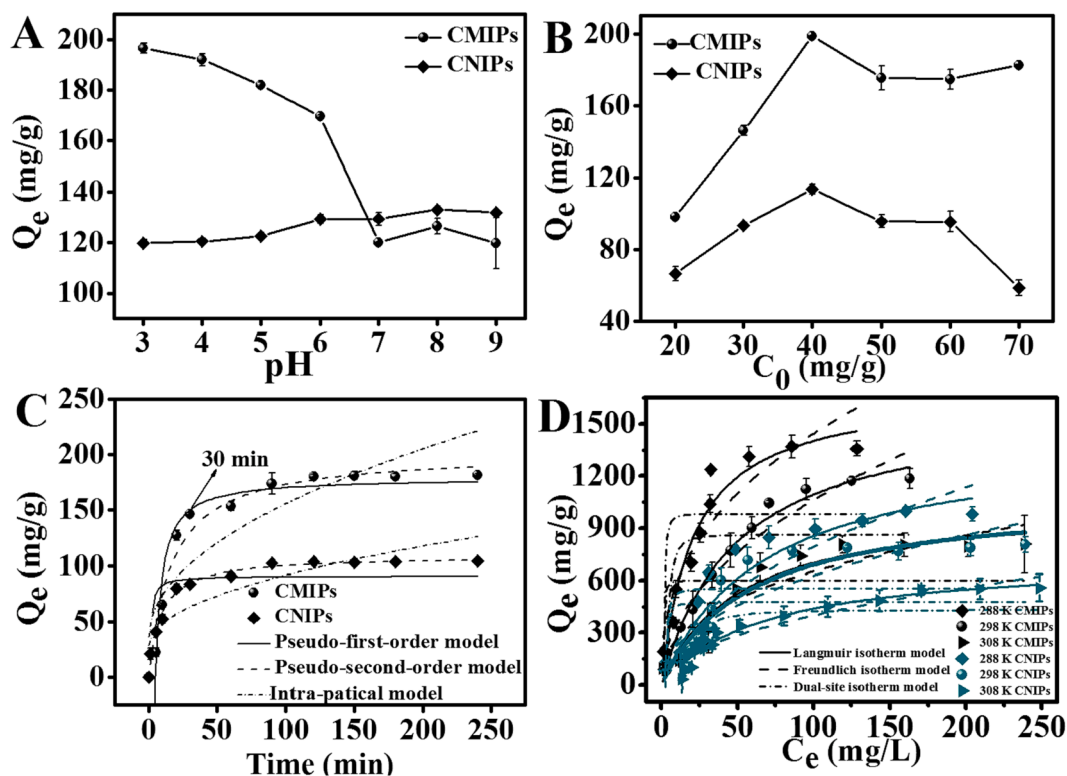


**Fig. 3.** Effect of pH (A) and concentration (B) on the adsorption of naringenin by CMIPs/CNIPs in aqueous solutions; (C) The kinetic models fitting plots of naringenin adsorption by CMIPs/CNIPs in aqueous solutions; (D) Three isotherm models of Langmuir, Freundlich, and dual-site of naringenin in aqueous solutions at 288, 298, and 308 K, respectively.

The related parameters and the correlation coefficients ($R^2$) were summarized in Table S1. As shown in Table S1, the adsorption of naringenin by CMIPs matched better with the pseudo-second-order model, evidenced by the higher $R^2$ value of 0.9665 than in the pseudo-first-order model ($R^2 = 0.9653$), indicating that the target molecules had different binding energies at the surface CMIPs. These results suggested

that the square of the number of unoccupied adsorption sites is a rate-limiting step in the adsorption process for naringenin.

*3.2.4. Adsorption isotherms*

The adsorption isotherm shows the relationship between the amount of adsorbate in a liquid and the amount of adsorption on a solid surface

at a specific temperature (Wang and Guo, 2020). To understand the adsorbent capacity, adsorption isotherms studies were carried out with the initial concentrations of naringenin from 20 to 400 mg/L at 288–308 K. The relationship between equilibrium adsorption amount $q_e$ and residual naringenin concentration $C_e$ is shown in Fig. 3D. As shown in Fig. 3D, the adsorption capacity increased quickly with the increase of naringenin concentration, and the equilibrium adsorption capacities of naringenin were 1311.6, 1123.7, and 804.8 mg/g at 288, 298, and 308 K, respectively. This indicated that the higher concentration gradient of naringenin could have facilitated the diffusion of naringenin molecules toward CMIPs. Compared to CMIPs, CNIPs had lower adsorption capacities, indicating that CMIPs possessed specific sites or specific functional groups on their surface that interacted with naringenin repeatedly due to the molecular imprinting effect (Ahmed et al., 2017). Additionally, low temperatures were found to be conducive to the naringenin adsorption, likely due to the enhanced mobility of naringenin at higher temperatures, which hindered the CMIP's effective capture of its molecules (Cui et al., 2020). To further clarify this process, three classical isotherm models, Langmuir (Eq. (9)), dual-site (Eq. (10)), and Freundlich models (Eq. (11)), were adopted.

$$q_e = \frac{Q_{max}K_L C_e}{1 + K_L C_e} \tag{9}$$

$$q_e = Q_{max}\left(1 + \frac{1}{2K_d C_e}\right) - Q_{max}\sqrt{\left(1 + \frac{1}{2K_d C_e}\right)^2 - 1} \tag{10}$$

$$q_e = K_f C_e^{\frac{1}{n}} \tag{11}$$

where $q_e$ and $c_e$ were the same as described before; $Q_{max}$ (mg/g) was the maximum adsorption capacity calculated from the models; $K_L$ (L/mg) was the Langmuir constant reflecting the affinity between the adsorbate and binding sites; $K_f$ and $n$ were the Freundlich constants.

As shown in Table S2, the values of $R^2$ in the Langmuir isotherm models were larger than those of Freundlich and dual-site models, which indicated that the adsorption process could be well described by the Langmuir isotherm model. This suggested that monolayer adsorption occurred and the active site in CMIPs was homogeneous distribution (Wang et al., 2021), which was consistent with the previous results of EDS. The maximal adsorption capacities of CMIPs were calculated to be 1698.14, 1628.05, and 1050.03 mg/g at 288, 298, and 308 K, respectively. These results suggested that the CMIPs have the potential as a promising adsorbent for the efficient adsorption of naringenin molecules.

### 3.2.5. Adsorption thermodynamics

To estimate the feasibility of the adsorption process and the change in energy, the adsorption thermodynamic parameters such as the Gibbs free energy ($\Delta G^0$), enthalpy change ($\Delta H^0$), and entropy change ($\Delta S^0$) were calculated according to Eqs. (12)–(14):

$$\Delta G^0 = \Delta H^0 - T\Delta S^0 \tag{12}$$

$$\Delta G^0 = -RTLn(K) \tag{13}$$

$$Ln(K) = \frac{\Delta S^0}{R} - \frac{\Delta H^0}{RT} \tag{14}$$

where $K$ represented the equilibrium constant; $T$ was the temperature (in Kelvin) during adsorption, and $R$ (8.3145 J/mol/K) was the ideal gas constant.

Calculation of the thermodynamics was carried out for the adsorbents at 288, 298, and 308 K and the related parameters were shown in Table S3. The negative values of the $\Delta H^0$ and $\Delta S^0$ indicated that the adsorption was exothermic and an entropy-decreasing process (Cui et al., 2018). The negative $\Delta G^0$ values and the decreased absolute $\Delta G^0$ values with raised temperatures indicated that the uptake of naringenin

was spontaneous and favorable at lower temperatures. Generally, the absolute $\Delta G^0$ value in the process of physical adsorption ($-20 \sim 0$ kJ mol$^{-1}$) was smaller than that of chemical adsorption ($-80 \sim -400$ kJ/mol) (Fu et al., 2015). Therefore, the adsorption of naringenin onto the CMIPs can be classified as physical adsorption, as evidenced by the $\Delta G^0$ values falling within the range of $-6.1 \sim -4.2$ kJ/mol.

### 3.3. Adsorption mechanism

To reveal the adsorption mechanism of CMIPs, the changes in functional groups on the CMIPs before and after naringenin adsorption were monitored by FT-IR and XPS. As shown in Fig. 2B, compared to naringenin, the stretching vibration of N—H had been weakened and broadened for the naringenin loaded on CMIPs, which was probably due to the generation of hydrogen bond between hydroxyl groups from naringenin and nitrogen-containing groups in CMIPs (Zhao et al., 2020). The elemental chemical composition and binding energy changes before and after adsorption were analyzed by XPS and the high-resolution spectra for C1s and O1s of naringenin were shown in Fig. 4. In Fig. 4A, there were four peaks in high-resolution C1s spectra of CMIPs. The binding energy peak at 284.97, 287.80, 288.92, and 290.35 eV was attributed to C—C, C—N, C=O, and the π–π* bonds, respectively. After adsorption, the π–π* bonds peaks from the pristine CMIPs at 290.18 eV shifted to lower values of 290.35 eV and the relative content increased from 1.58 % to 2.50 %, while the relative content of C—C decreased from 76.61 % to 74.38 % which revealed the π–π* interactions occur between the phenyl rings of naringenin molecules and that of CMIPs. The high-resolution spectrum of O1s (Fig. 4B) was de-convoluted into representative chemical groups of B-O-B, O—H, and C=O bonds, which emerged at binding energies of 531.65, 532.08, and 533.08 eV, respectively (Oprea et al., 2013). After adsorption, the relative content of O—H in CMIPs increased from 24.48 % to 25.80 %, while the relative content of B-O-B and C=O slightly decreased, possibly due to the abundant hydroxyl groups present in naringenin loaded onto the CMIPs. The C=O content, accounting for more than half that of the total chemical groups, indicated the crucial role played by APTES-MAA in the formation of the framework. Furthermore, the peaks of B-O-B, O—H and C=O remained almost unchanged before and after adsorption, indicating excellent stability of the CMIPs framework. These results demonstrated that prepared CMIPs had a strong affinity towards naringenin molecules through hydrogen bonding and π–π* interactions.

### 3.4. Selectivity and reusability

The adsorption selectivity of CMIPs was a vital index for evaluating the specific recognition of naringenin in actual complex samples. To investigate the selectivity of CMIPs, structurally similar flavonoids were selected including rutin, hesperidin, anthocyanin, and baicalin, with the structure shown in Fig. S2. Under the same adsorption conditions, the adsorption capacity of naringenin to CMIPs was significantly higher than that of other substrates (Fig. 4C). The selectivity of CMIPs mainly resulted from imprinted pores matched with the target molecules in shape, size, and distribution of functional groups (Zhao et al., 2020). As shown in Table S4, the selectivity factor ($k^{sel}$) for analogues was greater than 7. Especially, the $k^{sel}$ for anthocyanin reached 16. The poor affinity was ascribed to the lack of a carbonyl group for anthocyanin. Consequently, CMIPs had excellent selectivity for naringenin. $k^{sel}$ of CNIPs for analogues was between $2.0 \sim 2.5$. The selectivity of CMIPs was more targeted at the structure rather than the size-exclusion effect of the pore.

The regeneration of the CMIPs was also studied by performing consecutive adsorption–desorption cycles under the same conditions to evaluate its practical reusability. As shown in Fig. 4D, the adsorption capacity of CMIPs for naringenin only decreased slightly throughout the six adsorption–desorption cycles. After five cycles, the removal efficiency leveled to a stable value of 89 % (P > 0.05), which indicated that
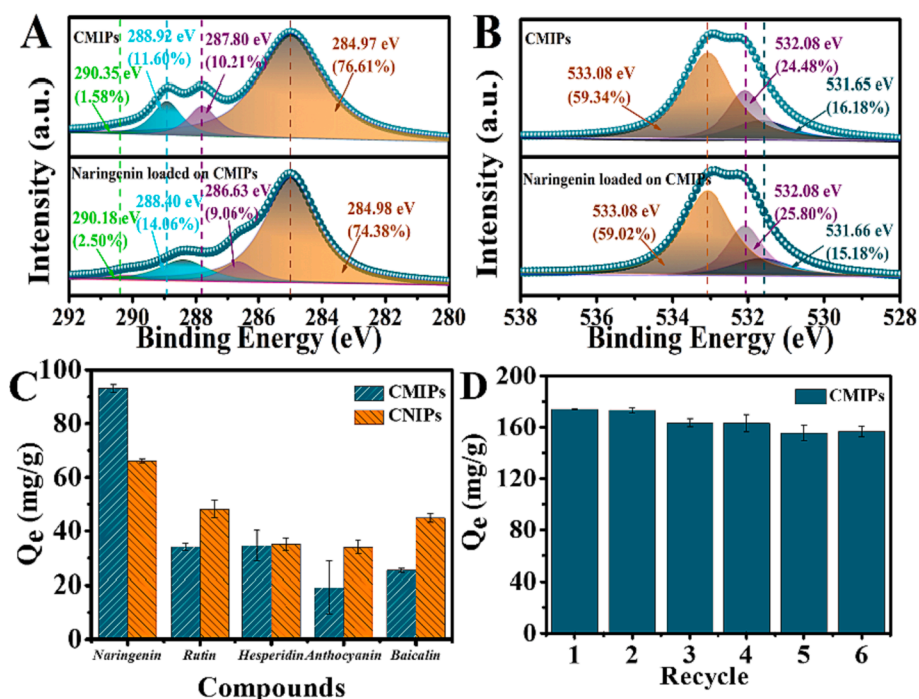
**Fig. 4.** (A) C1s and (B) O1s XPS spectra of CMIPs before and after naringenin adsorption; (C) Adsorption selectivity of CMIPs/CNIPs for naringenin; (D) Regeneration performance of CMIPs for naringenin adsorption.

the polymers had good stability and promising application prospects.

### 3.5. Application of the CMIPs to real samples

To further evaluate the specific selectivity of the CMIPs for practical applications, they were utilized to enrich naringenin in grapefruit peel extract. As depicted in Fig. 5, the retention time of the naringenin standard was observed at 13.42 min (Fig. 5a). After treatment with CMIPs (Fig. 5e), a significant decrease in the peak area of naringenin was detected, resulting in an extraction efficiency of nearly 70 % from grapefruit peel extract solution. In contrast, treatment with CNIPs (Fig. 5f) had a negligible impact on the peak area of naringenin. An 80 % alcohol extract of CMIPs and CNIPs was analyzed to determine if the ligand had desorbed from the adsorbents. As shown in Fig. 5b and c, the absence of any discernible peaks confirmed no ligand dissolution from the adsorbents. A comparison was made between these adsorbents and other commonly used methods for separating and purifying flavonoids in grapefruit peel extracts to evaluate their practical applications. As shown in Fig. 5B, the adsorption efficiency of CMIPs was higher than

that of other adsorbents, including ethylene benzene polymer AB-8, D101, cationic exchange resin, and active carbon. Notably, AB-8 and D101 exhibited a relatively high adsorption efficiency despite their ability to only form π–π* interactions with naringenin. This observation suggested that the π–π* interaction played a dominant role. After purification by CMIPs, the purity of naringenin reached ~90 %. Furthermore, the stability of CMIPs was important in practical applications. The leakage of boron in the alcohol extract of grapefruit peel after adsorption was determined by the inductively coupled plasma mass spectrometry (ICP-MS), and the boron element was not detected which indicated that the CMIPs had strong stability. Therefore, CMIPs can be used as an alternative to traditional adsorbents for the separation and purification of naringenin.

### 4. Conclusions

A strategy of fusion covalent organic frameworks and molecularly imprinted polymers was developed for preparing the CMIPs and used for the highly efficient enrich naringenin from grapefruit peels. The
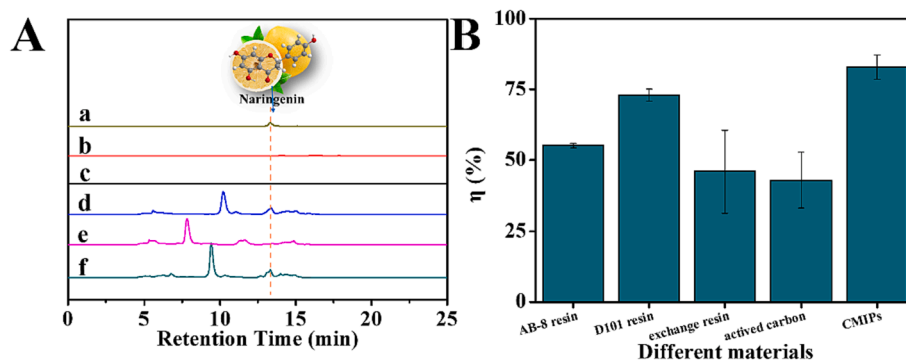


**Fig. 5.** (A) Chromatograms of grapefruit extract (a) the standard of naringenin; (b) 80 % alcohol extract of CMIPs; (c) 80 % alcohol extract of CNIPs; (d) Initial samples; (e) sample after extraction by CMIPs; (f) sample after extraction by CNIPs; (B) the adsorption efficiency of AB-8, D101, cationic exchange resin, active carbon and CMIPs.

characterization demonstrated that the naringenin was successfully imprinted and generated imprinted defective mesopores into the structure of CMIPs. The synergy effect between the MIPs and covalent organic building units endowing the CMIPs composites considerable mesopore structure and imprinted cavies thus displayed high adsorption capacity, fast adsorption rate, excellent selectivity, and stable reusability. The selective naringenin adsorption mechanism was based on π–π* interaction and hydrogen bond. Most importantly, the CMIPs exhibited excellent adsorption affinity in grapefruit peel extraction, achieving a purity of naringenin ~90 %. Additionally, CMIPs showed outstanding chemical stability and high resolution. Therefore, CMIPs can be used as an alternative to traditional adsorbents for the separation and purification of naringenin in practical applications. Moreover, the CMIPs synthesis strategy and the functional hybrid monomer of MIPs may provide some ideas for future studies.

## CRediT authorship contribution statement

**Xiumei Chen:** Conceptualization, Methodology, Writing – original draft, Data curation, Project administration. **Yingying Sheng:** Conceptualization, Methodology, Investigation, Writing – original draft, Data curation. **Jinxin Che:** Conceptualization, Methodology, Writing – review & editing, Supervision. **Okwong Oketch Reymick:** Investigation. **Nengguo Tao:** Methodology, Writing – review & editing, Supervision, Data curation, Project administration.

## Declaration of competing interest

The authors declare that they have no known competing financial interests or personal relationships that could have appeared to influence the work reported in this paper.

## Data availability

Data will be made available on request.

## Acknowledgements

## Appendix A. Supplementary data

Supplementary data to this article can be found online at https://doi.org/10.1016/j.fochx.2023.101107.

## References

Ahmed, M. B., Zhou, J. L., Ngo, H. H., Guo, W., Johir, M. A. H., Sornalingam, K., & Sahedur Rahman, M. (2017). Chloramphenicol interaction with functionalized biochar in water: Sorptive mechanism, molecular imprinting effect and repeatable application. *Science of the Total Environment, 609*, 885–895. https://doi.org/10.1016/j.scitotenv.2017.07.239

Bao, T., Wang, S., Zhang, N., & Zhang, J. (2021). Facile synthesis and immobilization of functionalized covalent organic framework-1 for electrochromatographic separation. *Journal of Chromatography A, 1645*, Article 462130. https://doi.org/10.1016/j.chroma.2021.462130

Barbosa, P. D. P. M., Ruviaro, A. R., Martins, I. M., Macedo, J. A., LaPointe, G., & Macedo, G. A. (2021). Enzyme-assisted extraction of flavanones from citrus pomace: Obtention of natural compounds with anti-virulence and anti-adhesive effect against *Salmonella enterica* subsp. enterica serovar Typhimurium. *Food Control, 120*, Article 107525. https://doi.org/10.1016/j.foodcont.2020.107525

Cui, Y., Kang, W., Qin, L., Ma, J., Liu, X., & Yang, Y. (2020). Magnetic surface molecularly imprinted polymer for selective adsorption of quinoline from coking wastewater. *Chemical Engineering Journal, 397*, Article 125480. https://doi.org/10.1016/j.cej.2020.125480

Cui, Z., Zhang, J., Xue, Y., & Duan, H. (2018). Size-dependent thermodynamics and kinetics of adsorption on nanoparticles: A theoretical and experimental study. *Langmuir, 34*, 3197–3206. https://doi.org/10.1021/acs.langmuir.7b04097

Du, Y., Calabro, D., Wooler, B., Kortunov, P., Li, Q., Cundy, S., & Mao, K. (2015). One step facile synthesis of amine-functionalized COF-1 with enhanced hydrostability. *Chemistry of Materials, 27*, 1445–1447. https://doi.org/10.1021/cm5032317

Fazary, A. E., Alshihri, A. S., Alfaifi, M. Y., Saleh, K. A., Elbehairi, S. E. I., Fawy, K. F., & Abd-Rabboh, H. S. M. (2016). Gibbs energies of protonation and complexation of platinum and vanadate metal ions with naringenin and phenolic acids: Theoretical calculations associated with experimental values. *The Journal of Chemical Thermodynamics, 100*, 7–21. https://doi.org/10.1016/j.jct.2016.04.005

Fu, J., Chen, Z., Wang, M., Liu, S., Zhang, J., Zhang, J., Han, R., & Xu, Q. (2015). Adsorption of methylene blue by a high-efficiency adsorbent (polydopamine microspheres): Kinetics, isotherm, thermodynamics and mechanism analysis. *Chemical Engineering Journal, 259*, 53–61. https://doi.org/10.1016/j.cej.2014.07.101

Gan, S., Tong, X., Zhang, Y., Wu, J., Hu, Y., & Yuan, A. (2019). Covalent organic framework-supported molecularly dispersed near-infrared dyes boost immunogenic phototherapy against tumors. *Advanced Functional Materials, 29*, 1902757. https://doi.org/10.1002/adfm.201902757

Gercek, E., Zengin, H., Erdem Erisir, F., & Yilmaz, O. (2021). Biochemical changes and antioxidant capacity of naringin and naringenin against Malathion toxicity in *Saccharomyces cerevisiae*. *Comparative Biochemistry and Physiology Part C: Toxicology & Pharmacology, 241*, Article 108969. https://doi.org/10.1016/j.cbpc.2020.108969

Grunenberg, L., Savasci, G., Terban, M. W., Duppel, V., Moudrakovski, I., Etter, M., Dinnebier, R. E., Ochsenfeld, C., & Lotsch, B. V. (2021). Amine-linked covalent organic frameworks as a platform for postsynthetic structure interconversion and pore-wall modification. *Journal of the American Chemical Society, 143*, 3430–3438.

Hao, S., Zhang, T., Fan, S., Jia, Z., & Yang, Y. (2021). Preparation of COF-TpPa1 membranes by chemical vapor deposition method for separation of dyes. *Chemical Engineering Journal, 421*, Article 129750. https://doi.org/10.1016/j.cej.2021.129750

Hatamluyi, B., Sadeghian, R., Malek, F., & Boroushaki, M. T. (2021). Improved solid phase extraction for selective and efficient quantification of sunset yellow in different food samples using a novel molecularly imprinted polymer reinforced by Fe₃O₄@UiO-66-NH₂. *Food Chemistry, 357*, Article 129782. https://doi.org/10.1016/j.foodchem.2021.129782

Liu, F., Ma, Z., Deng, Y., Wang, M., Zhou, P., Liu, W., Guo, S., Tong, M., & Ma, D. (2021). Tunable covalent organic frameworks with different heterocyclic nitrogen locations for efficient Cr(VI) reduction, Escherichia coli disinfection, and paracetamol degradation under visible-light irradiation. *Environmental Science & Technology, 55*, 5371–5381. https://doi.org/10.1021/acs.est.0c07857

Lu, H. S., Han, W. K., Yan, X., Chen, C. J., Niu, T., & Gu, Z. G. (2021). A 3D anionic metal covalent organic framework with soc topology built from octahedral Ti(IV) complex for photocatalytic reactions. *Angewandte Chemie*. https://doi.org/10.1002/anie.202102665

Mahmoud, A. M., Hernandez Bautista, R. J., Sandhu, M. A., & Hussein, O. E. (2019). Beneficial effects of citrus flavonoids on cardiovascular and metabolic health. *Oxidative Medicine and Cellular Longevity, 2019*, 5484138. https://doi.org/10.1155/2019/5484138

Motia, S., Bouchikhi, B., & El Bari, N. (2021). An electrochemical molecularly imprinted sensor based on chitosan capped with gold nanoparticles and its application for highly sensitive butylated hydroxyanisole analysis in foodstuff products. *Talanta, 223*, Article 121689. https://doi.org/10.1016/j.talanta.2020.121689

Nasir, A. M., Ishak, N. H., Said, M. S. M., & Dzahir, I. H. M. (2019). One-pot synthesis of molecular-imprinted membrane for selective extraction of caffeic acid. *Polymer Bulletin, 77*, 3953–3968. https://doi.org/10.1007/s00289-019-02935-4

Oprea, B., Radu, T., & Simon, S. (2013). XPS investigation of atomic environment changes on surface of B₂O₃–Bi₂O₃ glasses. *Journal of Non-Crystalline Solids, 379*, 35–39. https://doi.org/10.1016/j.jnoncrysol.2013.07.024

Pan, T., Lin, Y., Wu, Q., Huang, K., & He, J. (2020). Preparation of boronate-functionalized surface molecularly imprinted polymer microspheres with polydopamine coating for specific recognition and separation of glycoside template. *Journal of Separation Science*. https://doi.org/10.1002/jssc.202000125

Qi, Z., Lu, R., Wang, S., Xiang, C., Xie, C., Zheng, M., Tian, X., & Xu, X. (2021). Selective fluorometric determination of microcystin-LR using a segment template molecularly imprinted by polymer-capped carbon quantum dots. *Microchemical Journal, 161*, Article 105798. https://doi.org/10.1016/j.microc.2020.105798

Saad, E. M., El Gohary, N. A., Abdel-Halim, M., Handoussa, H., Mohamed El Nashar, R., & Mizaikoff, B. (2021). Molecularly imprinted polymers for selective extraction of rosmarinic acid from *Rosmarinus officinalis* L. *Food Chemistry, 335*, Article 127644. https://doi.org/10.1016/j.foodchem.2020.127644

Shen, Y. F., Yuan, F. F., Liu, X. Y., Huang, Y. P., & Liu, Z. S. (2019). Synergistic effect of organic-inorganic hybrid monomer and polyhedral oligomeric silsesquioxanes in a boronate affinity monolithic capillary/chip for enrichment of glycoproteins. *Mikrochimica Acta, 186*, 812. https://doi.org/10.1007/s00604-019-3938-z

Stabrauskiene, J., Marksa, M., Ivanauskas, L., & Bernatoniene, J. (2022). Optimization of naringin and naringenin extraction from *Citrus × paradisi* L. using hydrolysis and excipients as adsorbent. *Pharmaceutics, 14*. https://doi.org/10.3390/pharmaceutics14050890

Sun, J., Klechikov, A., Moise, C., Prodana, M., Enachescu, M., & Talyzin, A. V. (2018). A molecular pillar approach to grow vertical covalent organic framework nanosheets on graphene: Hybrid materials for energy storage. *Angewandte Chemie, 57*, 1034–1038. https://doi.org/10.1002/anie.201710502

Sun, Y., Gu, Y., & Jiang, Y. (2021). Adsorption behavior of a tri-functionalized imprinted resin with high selectivity for 5-sulfosalicylic acid: Batch experiments and DFT

calculation. *Journal of Hazardous Materials, 412*, Article 125271. https://doi.org/10.1016/j.jhazmat.2021.125271

Sun, Y., Xu, L., Waterhouse, G. I. N., Wang, M., Qiao, X., & Xu, Z. (2019). Novel three-dimensional electrochemical sensor with dual signal amplification based on $MoS_2$ nanosheets and high-conductive $NH_2$-MWCNT@COF for sulfamerazine determination. *Sensors and Actuators B: Chemical, 281*, 107–114. https://doi.org/10.1016/j.snb.2018.10.055

Tang, H., Zhang, S., Huang, T., Cui, F., & Xing, B. (2020). pH-dependent adsorption of aromatic compounds on graphene oxide: An experimental, molecular dynamics simulation and density functional theory investigation. *Journal of Hazardous Materials, 395*, Article 122680. https://doi.org/10.1016/j.jhazmat.2020.122680

Wang, J., & Guo, X. (2020). Adsorption isotherm models: Classification, physical meaning, application and solving method. *Chemosphere, 258*, Article 127279. https://doi.org/10.1016/j.chemosphere.2020.127279

Wang, S., Shao, R., Li, W., Li, X., Sun, J., Jiao, S., Dai, S., Dou, M., Xu, R., Li, Q., & Li, J. (2022). Three-dimensional ordered macroporous magnetic inverse photonic crystal microsphere-based molecularly imprinted polymer for selective capture of Aflatoxin B1. *ACS Applied Materials & Interfaces, 14*, 18845–18853. https://doi.org/10.1021/acsami.2c01014

Wang, Y., Chen, X., Hu, X., Wu, P., Lan, T., Li, Y., Tu, H., Liu, Y., Yuan, D., Wu, Z., Liu, Z., & Chew, J. W. (2021). Synthesis and characterization of poly(TRIM/VPA) functionalized graphene oxide nanoribbons aerogel for highly efficient capture of thorium(IV) from aqueous solutions. *Applied Surface Science, 536*, Article 147829. https://doi.org/10.1016/j.apsusc.2020.147829

Yang, S., Qian, J., Kuang, L., & Hua, D. (2017). Ion-imprinted mesoporous silica for selective removal of uranium from highly acidic and radioactive effluent. *ACS Applied Materials & Interfaces, 9*, 29337–29344. https://doi.org/10.1021/acsami.7b09419

Zhang, D., Wang, Y., Geng, W., & Liu, H. (2019a). Rapid detection of tryptamine by optosensor with molecularly imprinted polymers based on carbon dots-embedded covalent-organic frameworks. *Sensors and Actuators B: Chemical, 285*, 546–552. https://doi.org/10.1016/j.snb.2019.01.092

Zhang, H., Li, Z., Zhou, S., Li, S. M., Ran, H., Song, Z., Yu, T., & Yin, W. B. (2022). A fungal NRPS-PKS enzyme catalyses the formation of the flavonoid naringenin. *Nature Communications, 13*, 6361. https://doi.org/10.1038/s41467-022-34150-7

Zhang, J. W., Tan, L., Zhang, Y. Z., Zheng, G. C., Xia, Z. N., Wang, C. Z., Zhou, L. D., Zhang, Q. H., & Yuan, C. S. (2019b). Debittering of lemon juice using surface molecularly imprinted polymers and the utilization of limonin. *Journal of Chromatography B, 1104*, 205–211. https://doi.org/10.1016/j.jchromb.2018.11.025

Zhang, Z., Liu, Y., Huang, P., Wu, F. Y., & Ma, L. (2021). Polydopamine molecularly imprinted polymer coated on a biomimetic iron-based metal-organic framework for highly selective fluorescence detection of metronidazole. *Talanta, 232*, Article 122411. https://doi.org/10.1016/j.talanta.2021.122411

Zhao, Q., Zhang, H., Zhao, H., Liu, J., Liu, J., Chen, Z., Li, B., Liao, X., Regenstein, J. M., Wang, J., & Yang, X. (2020). Strategy of fusion covalent organic frameworks and molecularly imprinted polymers: A surprising effect in recognition and loading of cyanidin-3-*O*-glucoside. *ACS applied Materials & Interfaces, 12*, 8751–8760. https://doi.org/10.1021/acsami.9b21460